Remote sensing of wave-orbital velocities in the surfzone

Tyler McCormack [a,*], Julia Hopkins [a], Britt Raubenheimer [b], Steve Elgar [b], Katherine L. Brodie [c]

[a] Department of Civil and Environmental Engineering, Northeastern University, 110 Forsyth St, Boston, MA, 02115, USA
[b] Department of Applied Ocean Physics and Engineering, Woods Hole Oceanographic Institution, 266 Woods Hole Rd., Woods Hole, MA, 02543, USA
[c] Coastal and Hydraulics Laboratory, US Army Engineer Research and Development Center, 1261 Duck Rd, Duck, NC, 27949, USA

ABSTRACT

Wave-orbital velocities are estimated with particle image velocimetry (PIV) applied to rapid sequences of images of the surfzone surface obtained with a low-cost camera mounted on an amphibious tripod. Time series and spectra of the remotely sensed cross-shore wave-orbital velocities are converted to the depth of colocated acoustic Doppler velocimeters (ADVs), using linear finite depth theory. These converted velocities are similar to the velocities measured in situ (mean nRMSE for time series = 16% and for spectra = 10%). Small discrepancies between depth-attenuated surface and in situ currents may be owing to errors in the surface velocity measurements, uncertainties in the water depth, the vertical elevation of the ADVs, and the neglect of nonlinear effects when using linear finite depth theory. These results show the potential to obtain spatially dense estimates of wave velocities using optical near-field remote methods during field campaigns and continuous monitoring operations.

1. Introduction

Wave-orbital velocities are important for a range of nearshore processes, including generating shear stress on the seafloor (Madsen and Grant, 1976) that suspends sediment into the water column and moves sediment along the bed, thus causing bathymetric evolution (Fredsoe and Deigaard, 1992; Nielsen, 1992; van Rijn, 1993), and driving shoreward mass flux (Svendsen, 1984). Orbital velocities also can impact infrastructure (Hughes, 2004) and drive wave-energy converters (Wang, 2015; Lopes de Almeida et al., 2020). Although wave-orbital velocities can be measured with in situ current meters accurately (0.5–1.0%, Nortek; Lohrmann et al., 1994; Voulgaris and Trowbridge, 1998), it can be difficult to deploy and maintain sensors in the surfzone where waves are breaking (Thornton and Guza, 1986). To complement field data, numerical models of surfzone processes have been developed, many of which are limited by either phase averaging, depth averaging, computational capabilities, or some combination thereof. As a result of these simplifications, the typical errors for modeled orbital velocities relative to field observations are generally 10–20% (Grasmeijer and Ruessink, 2003; Torres-Freyermuth et al., 2007; Nam et al., 2020).

To address the limitations of in situ measurements and models, remote sensing methods have been developed to enable observations of mean flows in the surfzone (Holland et al., 2001; Chickadel et al., 2003; Puleo et al., 2003; Perkovic et al., 2009; Holman and Haller, 2013; Wilson et al., 2014; Dérian and Almar, 2017; Anderson et al., 2021; Rodríguez-Padilla et al., 2021; Dooley et al., 2024; references therein, and many others), providing greater spatial coverage than possible with in situ methods. However, there are disadvantages of remote methods. For example, optical remote observations measure velocity at the surface and require sufficient lighting and sea surface texture (e.g. bubbles, foam, ripples, Puleo et al., 2003; Piepmeier and Waters, 2004; de Vries et al., 2011). In the surfzone, surface flows may be different than mid-water column flows, especially in the cross-shore where there can be shoreward mass flux on the surface in the presence of breaking waves, and offshore-directed undertow in the mid-water column (Svendsen, 1984; Stive and Wind, 1986). Further, although remote methods are non-intrusive, the surface velocity may be affected by wind stress (Rodríguez-Padilla et al., 2021). The wind direction is relatively constant compared with the periodic orbital velocities, and thus wind shear on the surface can increase surface velocity when in the same direction and decrease the surface velocity when in the opposite direction (Xie, 2017). Other issues with remote methods are the computational costs of image processing methods such as particle image velocimetry (PIV, Baker et al., 2023; McIlvenny et al., 2023), for example, and error that can be introduced with rectifying image pixels into physical coordinates (Baker et al., 2023; Dooley et al., 2024).

---

* Corresponding author. 110 Forsyth St, Boston, MA, 02115, USA.
  E-mail address: mccormack.ty@northeastern.edu (T. McCormack).

Here, remote sensing of surfzone currents is extended to the estimation of cross-shore wave-orbital velocities. To estimate wave-orbital velocities remotely, velocity at the surface is measured by tracking breaking-wave-induced foam in sequences of images of the sea surface and corrected for depth attenuation using linear finite depth theory. Time series and power spectra of the depth-corrected surface velocities are compared with mid-water column velocities measured with in situ current meters. The accuracy of the estimated velocity is evaluated in different environmental conditions (e.g., water depth, wave height, and wind speed).

2. Materials and methods

2.1. Data collection

Observations were obtained in May 2015 in the surfzone of a relatively long, straight beach at the US Army Corp of Engineers Field Research Facility (FRF) in Duck, North Carolina. Four acoustic Doppler velocimeters (ADVs) were deployed along a cross-shore transect spanning the surfzone from ~2- to 4-m water depth (Fig. 1). The in situ ADVs were offshore, on top, and onshore of a ~0.75 m high sandbar (cross-shore position 225 m in Fig. 1). Each ADV had an accompanying colocated pressure sensor. All sensors were sampled at 2 Hz for the first 3072 s of every hour, and observations underwent quality control to remove spurious data (Elgar et al., 2001, 2005). In addition, a mobile amphibious tripod (CRAB, Birkemeier and Mason, 1984) that held a GoPro video camera (Hero 4 in 1080p at 30 frames per second) about 10.6 m above the seafloor (Fig. 2) transited along the array, stopping at each of the 4 locations to record images of the sea surface above the ADVs. All videos that contained an ADV near the center of the field of view of the camera were selected for analysis (Table 1), resulting in four case studies, one at each of the four stations. Ranges of offshore (17-m water depth) significant wave heights, peak periods, and mean wave directions were 0.5–1.5 m (Fig. 3A), 5–6 s (Fig. 3B), and 70° north to 30° south of shore normal (Fig. 3C), respectively. Nearby measured water levels were between high and mid-ebb tide (Fig. 3D), and average wind speeds (measured on a neighboring pier in ~6 m water depth) were from 5 to 10 m/s (Fig. 3E).

2.2. Image processing

The raw images (30 Hz sampling frequency) were corrected for distortion (Fig. 2B) caused by the wide-angle lens of the camera (Fig. 2A) using the open-source program Argus (Jackson et al., 2016) that employs a fisheye distortion model (Urban et al., 2015; Scaramuzza et al., 2006). To increase contrast and better define features on the water surface, images were preprocessed using a contrast limited adaptive histogram equalization (CLAHE) filter (Pizer et al., 1987) with a 64-pixel window size and global contrast stretching that varied depending on the lighting of the individual video. Particle image velocimetry (PIV, Raffel et al., 1988; Adrian, 1991; Perkovic et al., 2009; Dooley et al., 2024; and many others) with PIVlab in MATLAB (Thielicke and Stamhuis, 2014; Thielicke and Sonntag, 2021) was used to estimate velocities within a region of interest (ROI). The ROI was defined on the sea surface directly over the location of the ADV and pressure sensor as a rectangular region where PIV was performed, measuring 112 X 81 pixels in the cross- and alongshore directions, respectively (Fig. 2B). The ROI varied in size from 4.95 (Video 3) to 6.78 m^2 (Video 1, Table 1) depending on the distance from the camera on the CRAB to the water surface and to the ADV (Fig. 4). PIV was performed in three passes, starting with a 40- X 40-pixel interrogation area and a step size of 20 pixels in the first pass, followed by two passes using 16- X 16-pixel windows, each with a step size of 8 pixels. The processing resulted in a 13 (cross-shore) by 9 (alongshore) array of surface velocity vectors [pixels/frame] at every time step.

To relate pixel length to meters, the distance from the camera to the PIV ROI was calculated for each video using the triangle similarity method (Megalingam et al., 2016) accounting for the vertical distance from the camera to the water surface (estimated using water depth measured by the pressure sensor colocated with the ADV), the horizontal distance from the CRAB to the ADV (surveyed), and the width of the CRAB walkway (0.4 m) (Fig. 4). With the pixel-to-meters calibration, the surface velocities measured with PIV (U$_s$) were converted from pixels per frame to meters per second. Only the cross-shore component of the mid-water column velocity (U) and U$_s$ were considered owing to the shore-normal wave propagation direction within the camera field of view, because the alongshore spectral values were an order of magnitude lower than those of the cross-shore wave orbital velocities and below the noise floor of the PIV estimates.
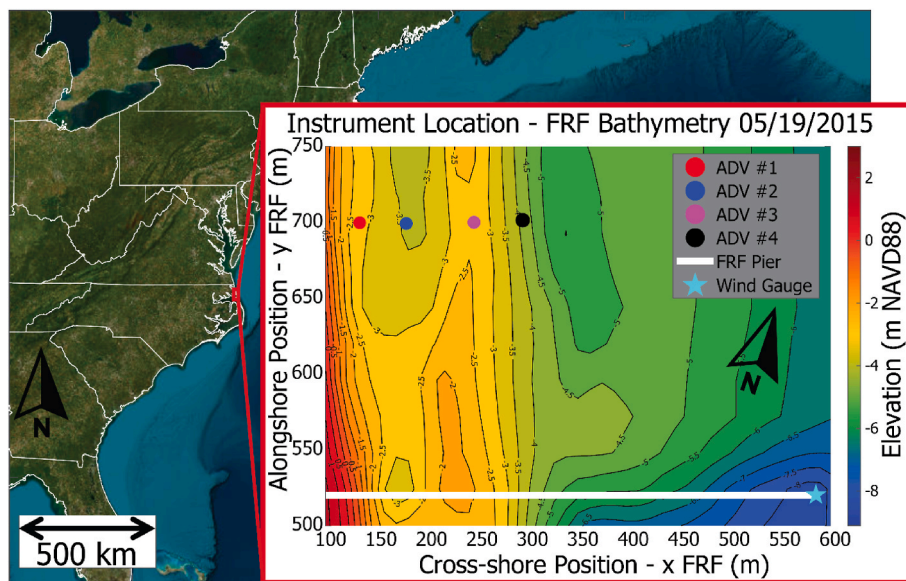

Fig. 1. Map of Eastern United States with an expanded view (red box) of the bathymetry (color scale on the right, 0.5 m contour curves) measured on May 19, 2015 as a function of alongshore and cross-shore position at the study site. Locations of the FRF pier (white rectangle), the ADVs (ADV #1 red, ADV #2 blue, ADV #3 magenta, ADV #4 black), and pier-end wind gage (cyan star) are overlaid on the bathymetry. The wave buoy used for incident wave conditions was in 17-m water depth located at X = 3715 and Y = 1433 m (not shown).
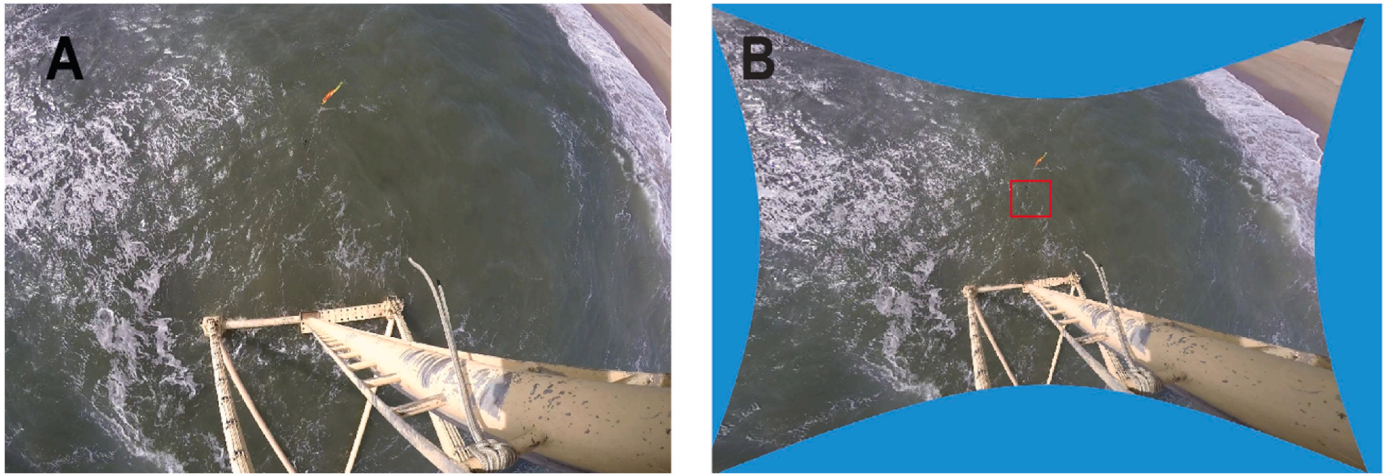
Fig. 2. (A) Raw view and (B) corrected-for-camera curvature views from the GoPro mounted on the CRAB with the PIV region of interest (red, panel B) colocated with the ADV from Case #1, recorded at 0 925 h EST on May 14, 2015.

Table 1
Details of the four videos used in the analysis. ADVs were approximately 0.78m above the seafloor in all cases.

Case #	ADV #	Video Start Time (EST)	Video Duration [mm:ss]	Mean Water Depth at ADV [m]	Z Location of ADV [m] (NAVD88)	Cross-shore Location (X FRF) [m]	H_s [m]	T_p [s]	PIV ROI [m^2]
1	1	14-May-2015 09:25 a.m.	15:35	2.20	−0.72	134	1.07	4.77	6.78
2	2	14-May-2015 10:02 a.m.	08:33	3.18	−2.72	180	1.07	4.77	6.45
3	3	15-May-2015 11:01 a.m.	12:40	1.59	−0.72	247	0.75	5.91	4.95
4	4	14-May-2015 12:01 p.m.	03:05	3.60	−2.72	295	1.47	4.96	6.50

The surface velocity vectors were processed to remove spurious values using an image contrast threshold that varied between videos (0.005–0.020) to eliminate vectors when the water surface was smooth with no trackable features or foam. In addition, vectors with a mean correlation coefficient of less than 0.6 were rejected. The remaining vectors in the ROI were spatially averaged over the entire area to calculate a single U_s measurement for each time step and were down-sampled from 30 to 2 Hz to match the sampling frequency of the ADVs and pressure sensors. Time lags between the video and ADV clocks (41, 2, 5, and 11 s for cases 1–4 respectively) were corrected by maximizing the velocity cross-correlation at zero lag. PIV measurement uncertainty was estimated using the mismatched pixel method (Sciacchitano et al., 2013) and converted to velocity. These uncertainties were averaged over each ROI and over the video duration, resulting in an average PIV uncertainty estimate for each case (0.21, 0.20, 0.19, 0.29 m/s).

3. Results

First, the camera-derived surface velocity (U_s) was compared with in situ velocity measurements (U) at the location of the ADV for four case studies (vertical shaded areas in Fig. 3). The surface currents U_s will differ from the mid-water column U because the ADV is 0.8–2.6 m below the mean surface (Table 1). Time series of U_s (red curves in Fig. 5) are similar to U (black curves in Fig. 5), although U_s has higher onshore-directed peaks. The normalized (by the maximum range of U) root mean square error (nRMSE) between U_s and U before any depth correction was applied was 28.36%, 25.34%, 10.08%, and 33.30% for the four cases, respectively (Fig. 5). The discrepancy between U_s and U increases as the mean water depth of the ADV increases.

The time series of U_s were converted to equivalent velocities at the depth of the ADV (U_c) using linear finite depth theory which accounts for velocity attenuation at depth, given by

$$U_c = U_s \frac{cosh(kz_c)}{cosh(kz_s)} \tag{1}$$

where U_c is the depth-converted velocity, U_s is the surface velocity measured by PIV, z_c is the height of the ADV above the seafloor (constant, z_c=0.78 m), and z_s is the time varying water depth. Here, k is the linear theory wavenumber associated with the peak period of the spectrum, and thus higher frequency motions are not attenuated sufficiently with depth, reducing correlations with midwater column ADVs. For example, the sharp onshore-directed peaks in the surface velocities are not attenuated sufficiently, leading to overprediction of mid-water column velocities during strong onshore flows (Fig. 6). Given the error introduced by using a single wavenumber in Equation (1), the depth-corrected U_c values are correlated ($0.54 < r^2 < 0.72$) with the corresponding measured wave orbital velocities at depth, with a mean bias of 0.13 m/s and mean normalized RMSE of 16.3% (Fig. 6).

The power spectral density (PSD) of the remotely sensed surface velocities were converted to spectra at the ADV depth also using linear finite depth theory, such that

$$P_{U_c}(f) = P_{U_s}(f) \frac{cosh^2(k(f)z_c)}{cosh^2(k(f)z_s)} \tag{2}$$

where $P_{U_c}(f)$ is the depth-converted PSD at frequency f for $0.05 < f < 0.50$ Hz, $P_{U_s}(f)$ is the PSD of the velocity at the surface, $k(f)$ is the wavenumber at each frequency calculated using mean water depth over the entire case, z_c is the height of the ADV above the seafloor (constant, z_c=0.78 m), and z_s is the mean water depth over the duration of the video. The PIV-estimated PSD at depth are similar to those estimated
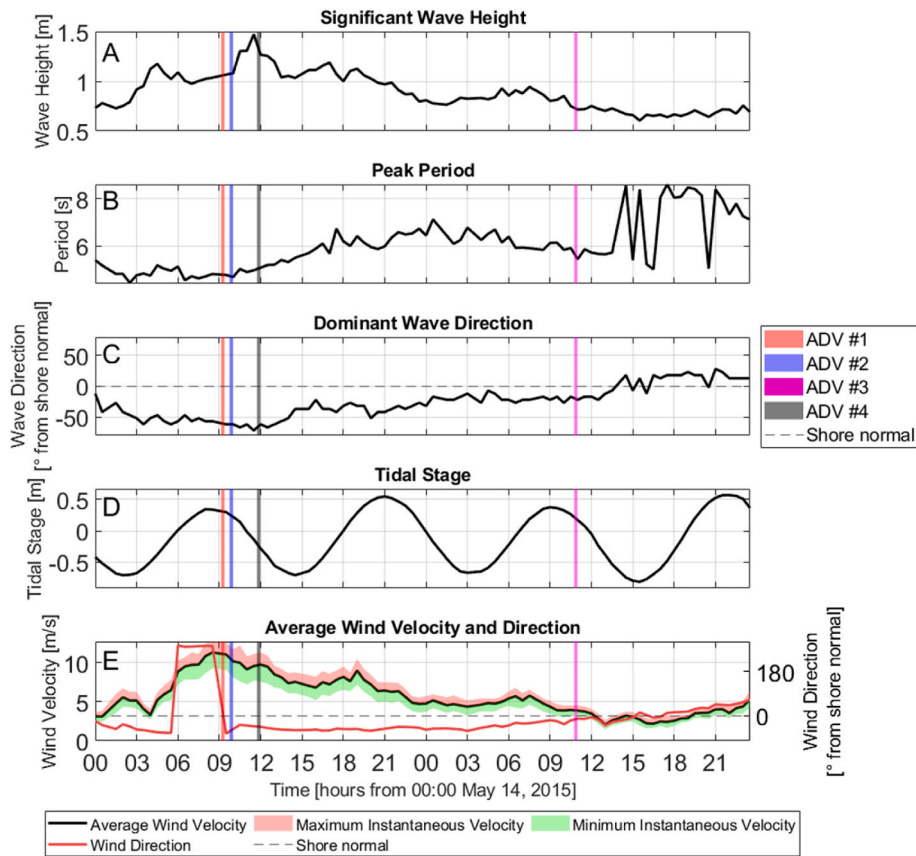
Fig. 3. Offshore (17m Datawell Waverider Buoy) (A) significant wave height, (B) peak period, (C) wave direction relative to true north (shore normal is 72°, black dashed line, north is negative, south is positive), (D) tidal range measured with a NOAA gage on the pier in ~6 m depth, and (E) pier-end wind speed (left vertical axis) and direction from north (right vertical axis) versus time since 00:00 May 14, 2015 (May 14–15). The colors in (E) represent maximum (red) and minimum (green) instantaneous wind speed over the 10-min averaging window. The shaded vertical bars indicate time periods corresponding to the case studies discussed here, colored by the ADV number for each case (legend on the right).
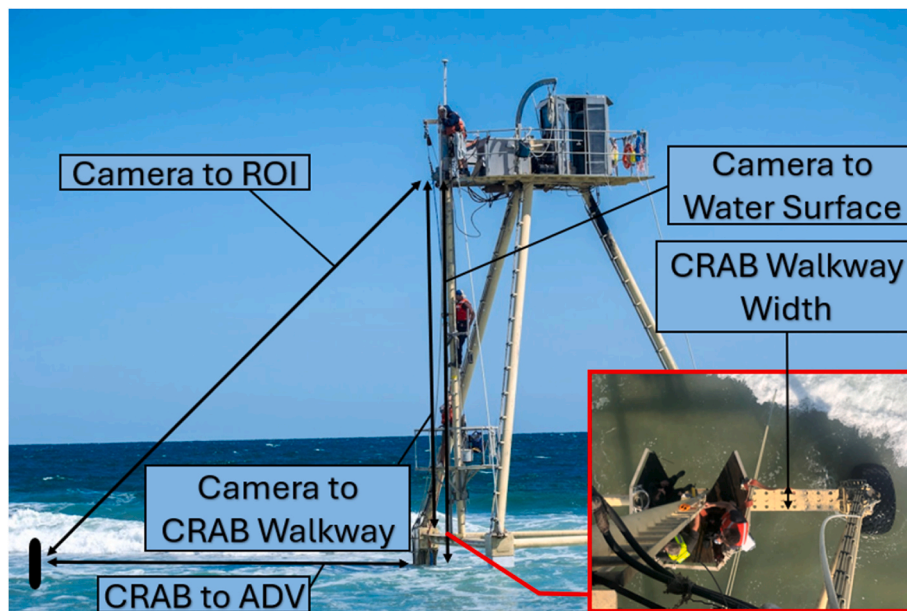

Fig. 4. Schematic of the distances used for the PIV image spatial calibration. The "Camera to Water Surface" and "CRAB to ADV" distances were used to calculate the "Camera to ROI" hypotenuse. The "Camera to CRAB Walkway" was used in addition to the "CRAB Walkway Width" in both pixels and meters to find the camera focal length using the triangle similarity method.
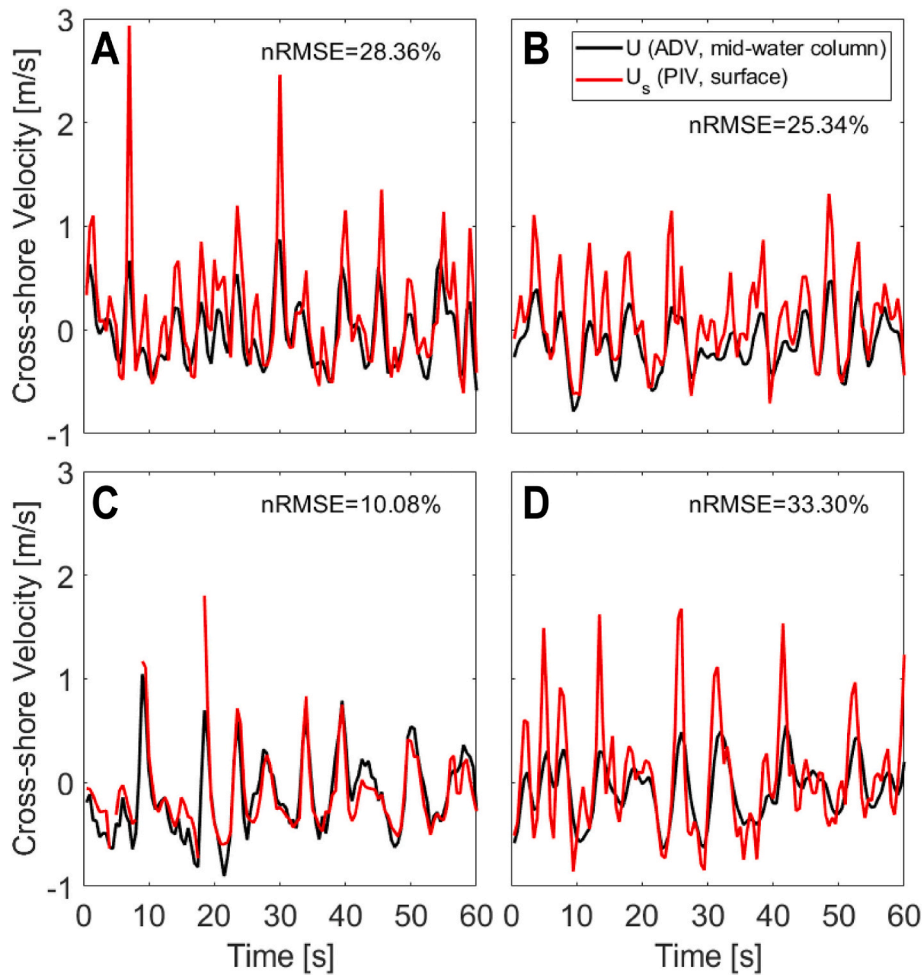
Fig. 5. Samples of PIV surface (red curves) and ADV mid-water column (black curves) cross-shore orbital velocities versus time for (A) Case #1, (B) Case #2, (C) Case #3, and (D) Case #4, (Case details in Table 1). Positive values are onshore directed. Data gaps are due to unreliable PIV measurements (mean correlation <0.6). nRMSE is calculated for the entire time series, not only the 60 s section shown here.

from the mid-water column observations (Fig. 7). The normalized (by the maximum range of $P_U(f)$) RMSE between $P_{U_c}(f)$ and $P_U(f)$ is less than 9% for 3 of the 4 cases (Fig. 7A–C), and 19% for Case #4 (Fig. 7D). Modifying the mean total water depth z_s in Equation (2) by ± 25% changes the RMSE by less than 5% (Fig. 7).

4. Discussion

The 10–20% RMSE between $P_{U_c}(f)$ and $P_U(f)$ is similar to errors in methods used to estimate near-bed orbital velocities from wave parameters to drive sediment transport models (Nam et al., 2020; Grasmeijer and Ruessink, 2003; Torres-Freyermuth et al., 2007; Kawamata and Kobayashi, 2023). Converting the surface velocity time series to mid-water column depth using only the wavenumber at the peak period was used to avoid errors associated with inverse Fourier transforms (e. g., phase shifts, Gibbs phenomenon). To quantify the effect of this simplification, Equation (2) was solved using only the wavenumber at the peak period of the surface velocities. The nRMSE between spectra of U and U_c increased by 9.5, 10.9, 1.1, and 11.3% for the four cases, respectively.

Other error sources that are applicable to both the time and frequency analyses include errors in PIV measurements, errors in water depth and ADV horizontal and vertical locations (e.g., causing errors in the rectification from pixels to physical coordinates), and ignoring nonlinear effects in the surfzone (Bonneton et al., 2018; Martins et al., 2020, 2023). PIV measurement errors can be caused by oblique camera

angle (Dooley et al., 2024) and reduced signal (foam) on the surface of wave troughs compared with wave crests. The latter is particularly evident in video 4 located at the most offshore location, which had the least breaking and consequently the least foam on the surface (Fig. 1). Video 4 also was recorded when the sun was directly overhead at midday (Table 1). The corresponding surface glare made the foam difficult to track, contributing to the largest error of the 4 videos (Fig. 5D, 6D and 7D). Many others have noted the decrease in PIV performance when there is insufficient surface texture (Puleo et al., 2003; Piepmeier and Waters, 2004; de Vries et al., 2011; Dooley et al., 2024). It is expected that poor surface texture and lighting, which varied across the four videos, are the primary contributions to PIV measurement uncertainty for the camera position and data considered here.

The bathymetry was measured by the mobile amphibious tripod, and the vertical locations of the ADVs were measured by SCUBA divers with hand-held tape measures. Both measurements are subject to error, which a sensitivity analysis showed could increase error in U_c by up to 5% if water depth accuracy is off by 25% (Fig. 7). Additionally, neglect of nonlinearities in the depth correction (Bonneton et al., 2018; Martins et al., 2020, 2023) can lead to errors. For the order (1 m) distance between the surface and the ADVs here, this error is relatively small.

The errors between $P_U(f)$ and $P_{U_c}(f)$ were not correlated with significant wave height, peak wave period, wave direction, average wind speed or direction, or water depth. The wave direction at the ADVs and the measured wind were both constant during each of the four videos. Thus, the influence of wind is expected to remain constant across all
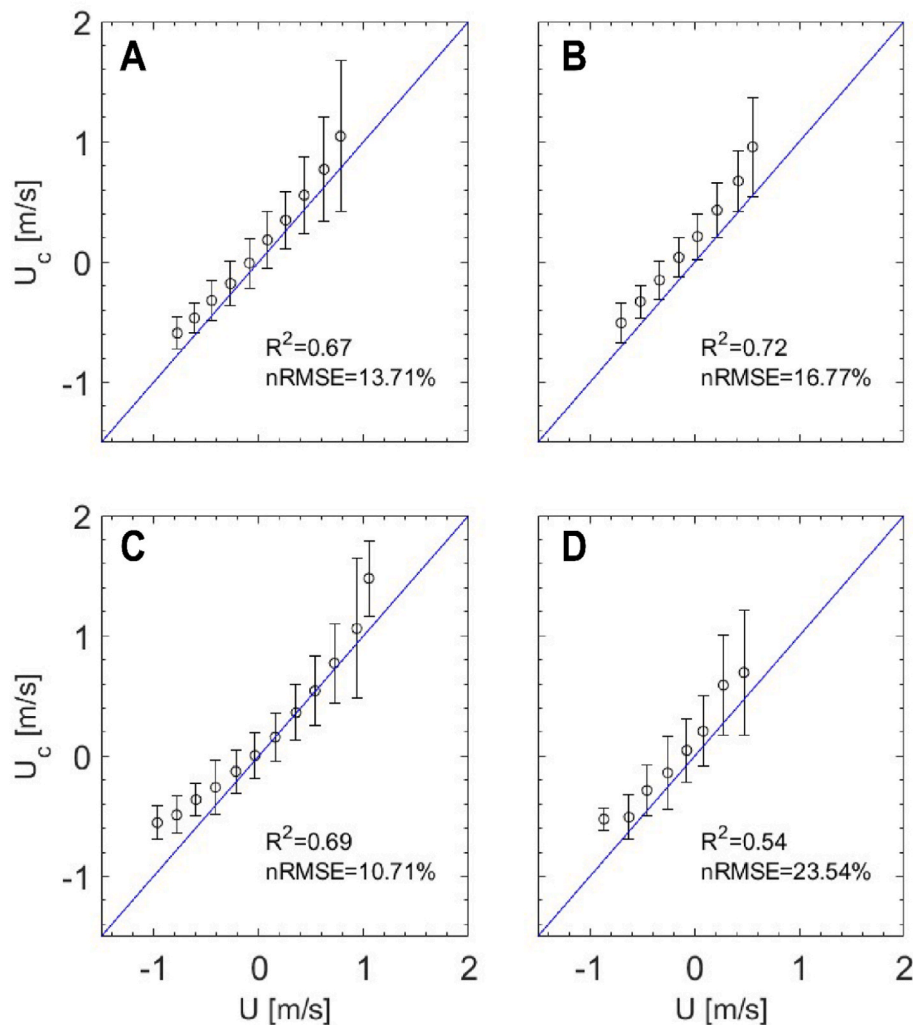
Fig. 6. Mean (circles) of U_c (surface velocity corrected for depth attenuation to the location of the mid-water column ADV) versus the velocity U measured by the mid-water column ADV. Circles are binned data (bin width = 0.2 m/s) and errors bars are one standard deviation of the 2 Hz wave-orbital velocities in each bin. The surface velocities estimated by PIV were converted to the velocity in mid-water column using the wavenumber of the power spectral peak frequency and linear finite depth theory. The blue lines are one-to-one perfect agreement line for (A) Case #1, (B) Case #2, (C) Case #3, and (D) Case #4 (Case details in Table 1). Positive values are onshore directed. Error metrics are from the raw (not the binned) data of the entire time series.

cases, despite not being able to quantify these effects without a full velocity profile. The methods presented here provide a new observation approach for measurement of surfzone velocities that may be useful for the study of nearshore hydrodynamic and sediment transport processes, model validation, and informing coastal design.

This study uses videos recorded from a camera mounted on a specialized surfzone-capable vehicle approximately 10 m above the water surface. It is possible to estimate surface velocities from shore- or drone-based cameras with sufficiently high resolution, even if the distance to the water surface is greater than 10 m. Recent studies using PIV in the surfzone achieved ~0.8 m resolution in the horizontal from a drone-based camera approximately 40 m above the surface (Dooley et al., 2024). The horizontal resolution of the method depends on a combination of camera resolution, PIV integration window and step size, and spatial averaging windows. Regardless of the camera-to-surface distance, this method can estimate orbital velocities for all surface gravity wavelengths (greater than a few centimeters) that are larger than the PIV resolution used.

5. Conclusion

Images of the sea surface were obtained with a low-cost camera

mounted on a mobile amphibious tripod at four locations spanning the surfzone in water depths from about 2 to 4 m. At each of the four locations, the field of view of the camera was above a mid-water column current meter. Time series and spectra of instantaneous (2 Hz) wave-orbital velocities derived from the sea-surface images using PIV are similar (mean normalized RMSE of 16% and 10% for time and frequency analysis, respectively) to the velocities measured by in situ mid-water column current meters when the surface velocity measurements are converted to the equivalent velocity at the depth of the in situ current meters using linear finite depth theory.

CRediT authorship contribution statement

Tyler McCormack: Writing – review & editing, Writing – original draft, Visualization, Validation, Methodology, Investigation, Formal analysis. **Julia Hopkins:** Writing – review & editing, Supervision, Conceptualization. **Britt Raubenheimer:** Writing – review & editing, Supervision, Funding acquisition, Data curation, Conceptualization. **Steve Elgar:** Writing – review & editing, Supervision, Funding acquisition, Data curation, Conceptualization. **Katherine L. Brodie:** Writing – review & editing, Funding acquisition, Data curation, Conceptualization.
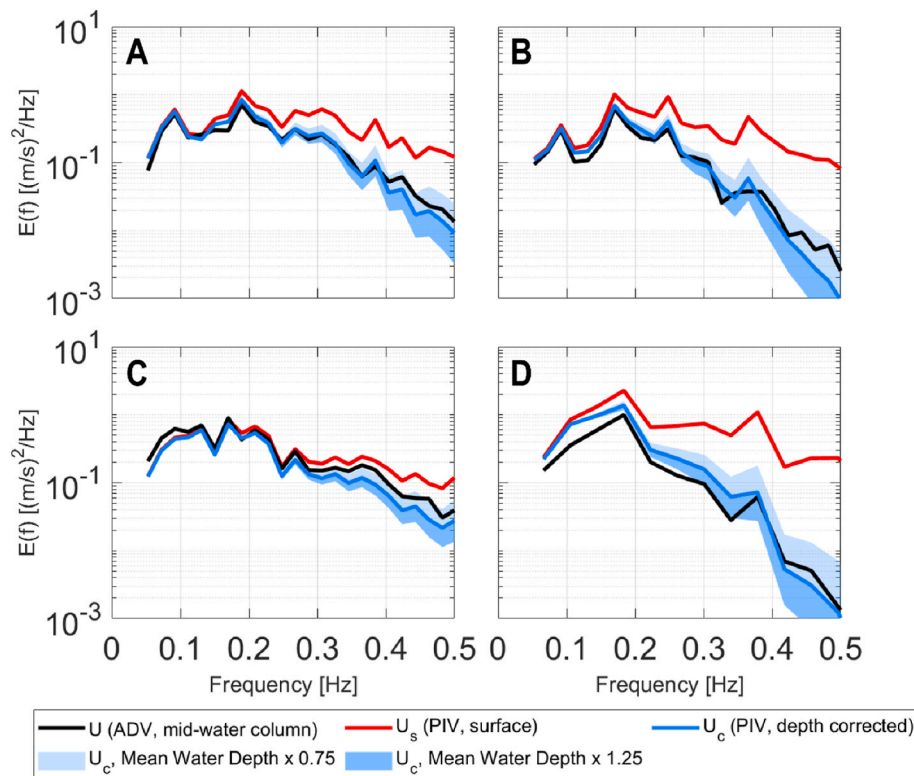
Fig. 7. Power spectral density of the PIV-estimated surface velocities U_s (red curves), surface velocities converted to the depth of the ADV U_c (blue curves), and velocities measured by an ADV in mid-water column U (black curves) for (A) Case #1, (B) Case #2, (C) Case #3, and (D) Case #4 (Case details in Table 1). Shaded areas are the ranges of U_c if the depth used in equation (2) is 25% less (light blue shaded area) or 25% more (dark blue shaded area) than the measured depth. There are 34, 19, 28, and 13 degrees of freedom for cases 1–4 respectively.

Declaration of competing interest

The authors declare that they have no known competing financial interests or personal relationships that could have appeared to influence the work reported in this paper.

Acknowledgements

Appendix A. Supplementary data

Supplementary data to this article can be found online at https://doi.org/10.1016/j.coastaleng.2024.104631.

Data availability

Data will be made available on request.

References

Adrian, R.J., 1991. Particle-Imaging techniques for experimental fluid mechanics. Annu. Rev. Fluid Mech. 23, 261–304. https://doi.org/10.1146/annurev.fl.23.010191.001401.

Anderson, D., Bak, A.S., Brodie, K.L., Cohn, N., Holman, R.A., Stanley, J., 2021. Quantifying optically derived two-dimensional wave-averaged currents in the surf zone. Rem. Sens. 13, 690. https://doi.org/10.3390/rs13040690.

Baker, C.M., Moulton, M., Palmsten, M.L., Brodie, K., Nuss, E., Chickadel, C.C., 2023. Remotely sensed short-crested breaking waves in a laboratory directional wave basin. Coast Eng. 183, 104327. https://doi.org/10.1016/j.coastaleng.2023.104327.

Birkemeier, W.A., Mason, C., 1984. The crab: a unique nearshore surveying vehicle. J. Survey Eng. 110 (1), 1–7. https://doi.org/10.1061/(ASCE)0733-9453(1984)110:1.

Bonneton, P., Lannes, D., Martins, K., Michallet, H., 2018. A nonlinear weakly dispersive method for recovering the elevation of irrotational surface waves from pressure measurements. Coast Eng. 138, 1–8. https://doi.org/10.1016/j.coastaleng.2018.04.005.

Chickadel, C.C., Holman, R.A., Freilich, M.H., 2003. An optical technique for the measurement of longshore currents. J. Geophys. Res.: Oceans 108. https://doi.org/10.1029/2003JC001774.

de Vries, S., Hill, D.F., de Schipper, M.A., Stive, M.J.F., 2011. Remote sensing of surf zone waves using stereo imaging. Coast Eng. 58, 239–250. https://doi.org/10.1016/j.coastaleng.2010.10.004.

Dérian, P., Almar, R., 2017. Wavelet-based optical flow estimation of instant surface currents from shore-based and UAV videos. IEEE Trans. Geosci. Rem. Sens. 55, 5790–5797. https://doi.org/10.1109/TGRS.2017.2714202.

Dooley, C., Elgar, S., Raubenheimer, B., Gorrell, L., 2024. Estimating surfzone currents with near-field optical remote sensing. J. Atmosph. Ocean. Tech., sub judice.

Elgar, S., Raubenheimer, B., Guza, R.T., 2001. Current meter performance in the surf zone. J. Atmos. Ocean. Technol. 18, 1735–1746.

Elgar, S., Raubenheimer, B., Guza, R.T., 2005. Quality control of acoustic Doppler velocimeter data in the surfzone. Meas. Sci. Technol. 16, 1889–1893.

Fredsoe, J., Deigaard, R., 1992. Mechanics of Coastal Sediment Transport. World Scientific Publishing Company.

Grasmeijer, B.T., Ruessink, B.G., 2003. Modeling of waves and currents in the nearshore parametric vs. probabilistic approach. Coast Eng. 49, 185–207. https://doi.org/10.1016/S0378-3839(03)00045-0.

Holland, K.T., Puleo, J.A., Kooney, T.N., 2001. Quantification of swash flows using video-based particle image velocimetry. Coast Eng. 44, 65–77. https://doi.org/10.1016/S0378-3839(01)00022-9.

Holman, R., Haller, M.C., 2013. Remote sensing of the nearshore. Ann. Rev. Mar. Sci 5, 95–113. https://doi.org/10.1146/annurev-marine-121211-172408.

Hughes, S.A., 2004. Wave momentum flux parameter: a descriptor for nearshore waves. Coast Eng. 51, 1067–1084. https://doi.org/10.1016/j.coastaleng.2004.07.025.

Jackson, B.E., Evangelista, D.J., Ray, D.D., Hedrick, T.L., 2016. 3D for the people: multi-camera motion capture in the field with consumer-grade cameras and open source software. Biology Open 5, 1334–1342. https://doi.org/10.1242/bio.018713.

Kawamata, S., Kobayashi, M., 2023. Empirical formulas for near-bed wave orbital velocity parameters involved in maximum wave load in random wave trains. Ocean Eng. 276, 114133. https://doi.org/10.1016/j.oceaneng.2023.114133.

Lohrmann, A., Cabrera, R., Kraus, N., 1994. Acoustic-Doppler velocimeter (ADV) for laboratory use. Proceedings of Fundamental and Advancements in Hydraulic Measurements and Experimentation.

Lopes de Almeida, J.P.P.G., Abrantes, J.R.C.B., Bento, J.G.S.E.S., 2020. A simplified model for expedient computational assessment of the novel REEFS wave energy converter power output. Renew. Energy 157, 43–54. https://doi.org/10.1016/j.renene.2020.04.128.

Madsen, O.S., Grant, W.D., 1976. Quantitative description of sediment transport by waves. Coastal Engineering Proceedings 1 (15), 64. https://doi.org/10.9753/icce.v15.64.

Martins, K., Bonneton, P., Mouragues, A., Castelle, B., 2020. Non-hydrostatic, non-linear processes in the surf zone. J. Geophys. Res.: Oceans 125, e2019JC015521. https://doi.org/10.1029/2019JC015521.

Martins, K., Bonneton, P., de Viron, O., Turner, I.L., Harley, M.D., Splinter, K., 2023. New perspectives for nonlinear depth-inversion of the nearshore using boussinesq theory. Geophys. Res. Lett. 50, e2022GL100498. https://doi.org/10.1029/2022GL100498.

McIlvenny, J., Williamson, B.J., Fairley, I.A., Lewis, M., Neill, S., Masters, I., Reeve, D.E., 2023. Comparison of dense optical flow and PIV techniques for mapping surface current flow in tidal stream energy sites. Int J Energy Environ Eng 14, 273–285. https://doi.org/10.1007/s40095-022-00519-z.

Megalingam, R.K., Shriram, V., Likhith, B., Rajesh, G., Ghanta, S., 2016. Monocular distance estimation using pinhole camera approximation to avoid vehicle crash and back-over accidents. In: 2016 10th International Conference on Intelligent Systems and Control (ISCO), pp. 1–5. https://doi.org/10.1109/ISCO.2016.7727017.

Nam, P.T., Staneva, J., Thao, N.T., Larson, M., 2020. Improved calculation of nonlinear near-bed wave orbital velocity in shallow water: validation against laboratory and field data. J. Mar. Sci. Eng. 8, 81. https://doi.org/10.3390/jmse8020081.

Nielsen, P., 1992. Coastal bottom boundary layers and sediment transport. In: Advanced Series on Ocean Engineering, 4. World Scientific Publishing Co. Pte. Ltd, Singapore, p. 340.

Nortek. Vector 300m Technical Specification.

Perkovic, D., Lippmann, T.C., Frasier, S.J., 2009. Longshore surface currents measured by Doppler radar and video PIV techniques. IEEE Trans. Geosci. Rem. Sens. 47, 2787–2800. https://doi.org/10.1109/TGRS.2009.2016556.

Piepmeier, J.A., Waters, J., 2004. Analysis of stereo vision-based measurements of laboratory water waves. In: IGARSS 2004. 2004 IEEE International Geoscience and Remote Sensing Symposium. Presented at the IGARSS 2004. 2004 IEEE International Geoscience and Remote Sensing Symposium, vol. 5, pp. 3588–3591. https://doi.org/10.1109/IGARSS.2004.1370487.

Pizer, S.M., Amburn, E.P., Austin, J.D., Cromartie, R., Geselowitz, A., Greer, T., ter Haar Romeny, B., Zimmerman, J.B., Zuiderveld, K., 1987. Adaptive histogram equalization and its variations. Comput. Vis. Graph Image Process 39, 355–368. https://doi.org/10.1016/S0734-189X(87)80186-X.

Puleo, J.A., Farquharson, G., Frasier, S.J., Holland, K.T., 2003. Comparison of optical and radar measurements of surf and swash zone velocity fields. J. Geophys. Res.: Oceans 108. https://doi.org/10.1029/2002JC001483.

Raffel, M., Willert, C.E., Scarano, F., Kähler, C.J., Wereley, S.T., Kompenhans, J., 2018. Particle Image Velocimetry: A Practical Guide. Springer.

Rodríguez-Padilla, I., Castelle, B., Marieu, V., Bonneton, P., Mouragues, A., Martins, K., Morichon, D., 2021. Wave-filtered surf zone circulation under high-energy waves derived from video-based optical Systems. Rem. Sens. 13, 1874. https://doi.org/10.3390/rs13101874.

Scaramuzza, D., Martinelli, A., Siegwart, R., 2006. A toolbox for easily calibrating omnidirectional cameras. In: 2006 IEEE/RSJ International Conference on Intelligent Robots and Systems. Presented at the 2006. IEEE/RSJ International Conference on Intelligent Robots and Systems, pp. 5695–5701. https://doi.org/10.1109/IROS.2006.282372.

Sciacchitano, A., Wieneke, B., Scarano, F., 2013. PIV uncertainty quantification by image matching. Meas. Sci. Technol. 24, 045302. https://doi.org/10.1088/0957-0233/24/4/045302.

Stive, M.J.F., Wind, H.G., 1986. Cross-shore mean flow in the surf zone. Coast Eng. 10, 325–340. https://doi.org/10.1016/0378-3839(86)90019-0.

Svendsen, I.A., 1984. Mass flux and undertow in a surf zone. Coast Eng. 8, 347–365. https://doi.org/10.1016/0378-3839(84)90030-9.

Thielicke, W., Sonntag, R., 2021. Particle image velocimetry for MATLAB: accuracy and enhanced algorithms in PIVlab. J. Open Res. Software 9. https://doi.org/10.5334/jors.334.

Thielicke, W., Stamhuis, E.J., 2014. PIVlab – towards user-friendly, affordable and accurate digital particle image velocimetry. MATLAB 2, e30. https://doi.org/10.5334/jors.bl.

Thornton, E.B., Guza, R.T., 1986. Surf zone longshore currents and random waves: field data and models. J. Phys. Oceanogr. 16, 1165–1178.

Torres-Freyermuth, A., Losada, I.J., Lara, J.L., 2007. Modeling of surf zone processes on a natural beach using Reynolds-Averaged Navier-Stokes equations. J. Geophys. Res.: Oceans 112. https://doi.org/10.1029/2006JC004050.

Urban, S., Leitloff, J., Hinz, S., 2015. Improved wide-angle, fisheye and omnidirectional camera calibration. ISPRS J. Photogrammetry Remote Sens. 108, 72–79. https://doi.org/10.1016/j.isprsjprs.2015.06.005.

van Rijn, L.C., 1993. Principles of Sediment Transport in Rivers, Estuaries and Coastal Seas. Aqua Publications, Amsterdam.

Voulgaris, G., Trowbridge, J.H., 1998. Evaluation of the acoustic Doppler velocimeter (ADV) for turbulence measurements. J. Atmos. Ocean. Technol. 15, 272–289. https://doi.org/10.1175/1520-0426(1998)015<0272:EOTADV>2.0.CO;2.

Wang, Y.-L., 2015. Design of a cylindrical buoy for a wave energy converter. Ocean Eng. 108, 350–355. https://doi.org/10.1016/j.oceaneng.2015.08.012.

Wilson, G.W., Özkan-Haller, H.T., Holman, R.A., Haller, M.C., Honegger, D.A., Chickadel, C.C., 2014. Surf zone bathymetry and circulation predictions via data assimilation of remote sensing observations. J. Geophys. Res.: Oceans 119, 1993–2016. https://doi.org/10.1002/2013JC009213.

Xie, Z., 2017. Numerical modelling of wind effects on breaking waves in the surf zone. Ocean Dynam. 67, 1251–1261. https://doi.org/10.1007/s10236-017-1086-8.